Journal of Computer Assisted Tomography
Issue: Volume 24(1), January/February 2000, pp 2-8

Publication Type: [Special Article]
ISSN: 0363-8715
Accession: 00004728-200001000-00002
Keywords: Magnetic resonance imaging, High resolution, Brain, Microanatomy, Atlas and atlases

[Special Article]

Ultra High Resolution Imaging of the Human Head at 8 Tesla: 2K × 2K for Y2K

Robitaille, Pierre-Marie L.; Abduljalil, Amir M.; Kangarlu, Allahyar

Author Information

From the Center for Advanced Biomedical Imaging, Department of Radiology, The Ohio State University, Columbus, Ohio, U.S.A. Address correspondence and reprint requests to Dr. P.-M. Robitaille, MRI Facility, 1630 Upham Dr., Columbus, OH 43210, U.S.A.

Abstract

Purpose: To acquire ultra high resolution MRI images of the human brain at 8 Tesla within a clinically acceptable time frame.

Method: Gradient echo images were acquired from the human head of normal subjects using a transverse electromagnetic resonator operating in quadrature and tuned to 340 MHz. In each study, a group of six images was obtained containing a total of 208 MB of unprocessed information. Typical acquisition parameters were as follows: matrix = 2,000 × 2,000, field of view = 20 cm, slice thickness = 2 mm, number of excitations (NEX) = 1, flip angle = 45°, TR = 750 ms, TE = 17 ms, receiver bandwidth = 69.4 kHz. This resulted in a total scan time of 23 minutes, an in-plane resolution of 100 µm, and a pixel volume of 0.02 mm^3.

Results: The ultra high resolution images acquired in this study represent more than a 50-fold increase in in-plane resolution relative to conventional 256 × 256 images obtained with a 20 cm field of view and a 5 mm slice thickness. Nonetheless, the ultra high resolution images could be acquired both with adequate image quality and signal to noise. They revealed numerous small venous structures throughout the image plane and provided reasonable delineation between gray and white matter.

Discussion: The elevated signal-to-noise ratio observed in ultra high field magnetic resonance imaging can be utilized to acquire images with a level of resolution approaching the histological level under in vivo conditions. However, brain motion is likely to degrade the useful resolution. This situation may be remedied in part with cardiac gating. Nonetheless, these images represent a significant advance in our ability to examine small anatomical features with noninvasive imaging methods.

INTRODUCTION

The first magnetic resonance imaging experiments were conducted with nuclear magnetic resonance (NMR) line scanning (1) and projection reconstruction (2) methods. While these methods established the feasibility of the magnetic resonance imaging (MRI) approach, they were characterized with relatively low spatial resolution (1,2). Nonetheless, technological advancements in gradient design (3) and spatial encoding methods (4,5) soon permitted an increase in achievable spatial resolution, thereby greatly improving the radiological utility of MRI methods.

The need for enhanced spatial resolution in magnetic resonance arises from the desire to more precisely visualize small structures both on conventional and angiographic images. Increased spatial resolution also results in reduced susceptibility artifacts in gradient echo based MRI imaging in part due to the associated increases in receiver bandwidths (6,7). In addition, enhanced spatial resolution leads to superior image interpolation required in generating MR angiograms (MRA).

Unfortunately, since magnetic resonance is an inherently insensitive technique, image resolution cannot be continuously increased without significantly compromising image quality and signal to noise (8–12). As these two characteristics progressively deteriorate, the ability to detect the structure of interest, or the visibility, also degrades (9). Visibility (V) can be defined as the product of the contrast-to-noise ratio (CNR) and the square root of the number of pixels (p) occupied by the object of interest (9). It is expressed as follows: V = CNR [square root]p. The importance of determining appropriate spatial resolution based on visibility rather than signal-to-noise criteria alone has been addressed (9).

addressed (9).

At 1.5 Tesla, increases in spatial resolution have often been associated with the use of specialized local surface (13) or phased array (14) radio frequency (RF) coils in order to maximize the available signal to noise at this field strength. In addition, signal processing methods may help enhance signal to noise while preserving, as much as possible, edge definition (15,16). Using a combination of these approaches, excellent high resolution images have been obtained from the human skin (17), the extremities and cartilage (18–20), the trabecular bone (21,22), the inner ear (23–27), the eye (28–31), and the facial nerves (32–34). Increased spatial resolution has also proven valuable in MRA studies where higher resolution 3D data sets provide improved vessel visualization (9,35,36). Indeed, increased spatial resolution leads not only to the visualization of more vessels but also in the ability to differentiate progressively smaller structures. It is known for instance that vessel visibility is determined by the position of the structure of interest within the voxel grid (35). Vessels contained entirely within one voxel are thus brighter than when positioned between voxels. This is a partial volume effect that can be reduced with increased matrix size. Nonetheless, as resolution continues to increase, signal to noise begins to degrade to such an extent that visibility becomes compromised and the number of vessels observed no longer continues to increase (35). Similarly, while high resolution approaches increase functional localization in functional MRI by reducing partial volume effects, this is associated both with a significant increase in scan times and a reduction in signal to noise (37).

Despite limitations in signal to noise even with high field (HF) systems operating at 1.5 Tesla, excellent high resolution studies of the human brain have been conducted at this field strength. Using phased array detectors and an automated intensity correction algorithm, for instance, Wald et al. (38) have been able to obtain good spoiled gradient recalled volume acquisition images. In these studies, an in-plane pixel size of 0.47–0.66 mm was obtained using a 0.7 mm slice thickness. Alternatively, using a fast spin echo approach, these authors (38) were able to obtain 512 × 512 images with an in-plane resolution of 0.27–0.33 mm with a 1.5–3 mm slice thickness and an acquisition time of only 8.5 minutes. Similarly, Feinberg et al. (39), using the gradient-SE (GRASE) technique and partial k-space sampling, were able to obtain 2D 1,024 matrix images of the human head in only 4 minutes, 20 seconds. The resulting images contained a 0.28 × 0.27 mm in-plane resolution from a 4 mm slice and displayed many small anatomic structures including the cochlea of the inner ear, vascular details, and the cranial nerves (39).

Given available field strength and total acquisition times, the aforementioned studies illustrate the potential of high resolution MRI. This conclusion can be further amplified by work performed at 4.1 Tesla (40,41) where high resolution modified driven equilibrium Fourier transform (MDEFT) images were obtained using a 512 × 512 matrix. These images had a 400–500 µm in-plane resolution from a 5 mm slice and revealed exquisite anatomical detail and gray/white matter contrast. Moreover, they display remarkable signal to noise in very high field (VHF) MRI, despite the use of standard volumetric head coils (40).

Recently, a series of 1K × 1K gradient echo images with a 200 µm in-plane resolution (42,43) have been obtained from the human head at 8 Tesla (44,45) using standard transverse electromagnetic (TEM) volumetric coils (40,46). These images display good in-plane resolution and enhancement of the venous vasculature (42,43). In addition, they highlight the tremendous magnetic susceptibility obtained at ultra high field (UHF) strengths. The 8 Tesla images also revealed that sufficient signal to noise was present at this field strength to further enhance image resolution. As such, and in order to herald the arrival of the new millenium, a group of ultra high resolution images were acquired from a 20 cm field of view (FOV) with a 2,000 × 2,000 matrix and a 2,000 µm slice thickness. The resulting images were obtained in 23 minutes and have a 100 µm in-plane resolution.

MATERIALS AND METHODS

Ultra high resolution gradient recalled echo images were acquired at 340 MHz using an 8 Tesla instrument. The design and assembly of this system has previously been described in detail (45,46). Briefly, however, it consists of an 8 Tesla/80 cm superconducting magnet manufactured by Magnex Scientific (Abingdon, England). This magnet is positioned within a magnetic shield constructed from 240,000 kg of annealed low carbon steel (grade 1006). Using a combination of superconductive shims located within the cryostat and resistive shims located in a specialized shim insert (45), the 8 Tesla magnet achieved a homogeneity of 5.13 ppm over a 40 cm diameter spherical volume established on a 12-plane plot. The gradient system utilized in these studies consists of an asymmetric torque free gradient insert (47) for dedicated head imaging (Magnex Scientific). This gradient set is driven by TECHRON 8745 amplifiers provided by Crown International (Elkhart, IN, U.S.A.). These amplifiers are capable of delivering 320 V/400 A on each gradient axis.

All images in this study were acquired with a Bruker AVANCE console (Billerica, MA, U.S.A.). This console is a four transmitter/four receiver system. It is equipped with Bruker Paravision Software and is able to support basic acquisition sequences for ultrafast imaging, broadline imaging, 3D imaging, angiography, and spectroscopy. The RF front end of the 8 Tesla system is comprised of a high power TR switch (Hill Engineering, Topsfield, MA, U.S.A.). Nonmagnetic narrowband GaAs field effect transitor (FET) preamplifiers (Advanced Receiver Research, Harwinton,

CT, U.S.A.) complete the front end allowing close proximity of the RF front end to the NMR coil. The quality of the receiver chain with the Bruker AVANCE console was measured by examining the noise performance using a liquid nitrogen dip test. This established that the complete receive path had a noise figure of 1.68 ± 0.21 including the TR switch (sweep width = 30 kHz; block size= 1k real, 1k imaginary; maximal receiver gain).

Radio frequency power at 340 MHz was provided by RF amplifiers constructed specifically for this project by CPC (Communication Power Corporation, Brentwood, NY, U.S.A.). Images were acquired with a TEM volumetric head coil (40,46). This coil was designed to operate in quadrature and was constructed from a group of 16 TEM struts enclosed in a copper shield.

Gradient recalled echo images were acquired in 23 minutes using standard imaging software (Bruker). Imaging parameters were as follows: sequence = gradient echo, matrix size = 2,000 × 2,000, slice thickness = 2,000 µm, FOV = 20 cm, in-plane resolution = 100 µm, TR = 750 ms, TE = 17 ms, receiver bandwidth = 69.4 kHz, slices = 6, NEX = 1, flip angle = 45°.

A complementary group of images was also acquired in 6.4 minutes at 1.5 Tesla using a GE Horizon Signa (Milwaukee, WI, U.S.A.) scanner operating with a standard GE high pass birdcage head coil operating in quadrature. Imaging parameters at 1.5 Tesla were as follows: sequence = gradient echo, matrix = 512 × 512, slice thickness = 2,000 µm, FOV = 20 cm, in-plane resolution = 390 µm, TR= 750 ms, TE = 17 ms, receiver bandwidth = 32 kHz, slices = 8, NEX = 1, flip angle = 45°.

RESULTS

A gradient echo image obtained from a normal volunteer at 1.5 Tesla using a 512 × 512 matrix is displayed in Fig. 1A. This image was obtained with a 2 mm slice thickness and a 20 cm FOV resulting in an in-plane resolution of 390 µm. A section of this image is displayed with a 10-fold magnification in Fig. 1B. Note that at 1.5 Tesla, the use of a 0.30 mm^3 pixel volume, in combination with a nonfully relaxed gradient echo acquisition scheme and a standard RF head coil, resulted in poor signal-to-noise performance. Indeed, the signal to noise in Fig. 1 was on the order of 6:1.

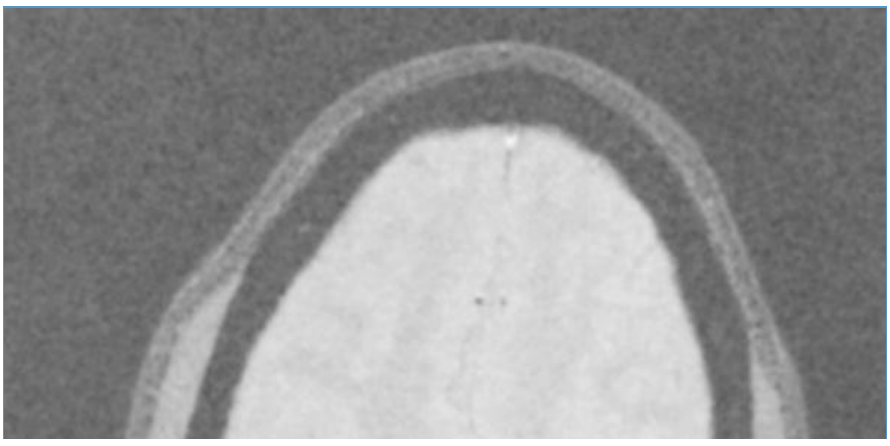

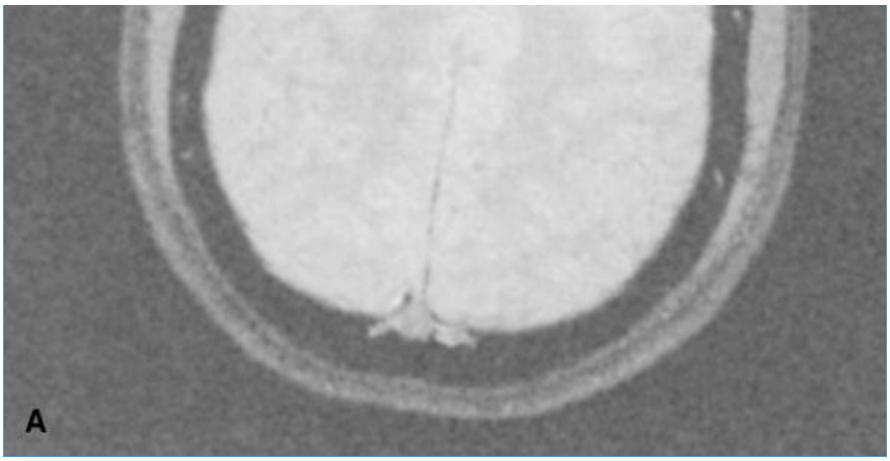

FIG. 1. A: Axial gradient recalled echo image acquired in 6.4 min at 1.5 Tesla using a standard GE quadrature head coil (matrix = 512 × 512, slice thickness = 2,000 µm, FOV = 20 cm, in-plane resolution = 390 µm, TR = 750 ms, TE = 17 ms, receiver bandwidth = 32 kHz, slices = 8, NEX = 1, flip angle = 45°. **B:** Expanded view of the image displayed in (A). This image has a signal to noise of only 6:1.

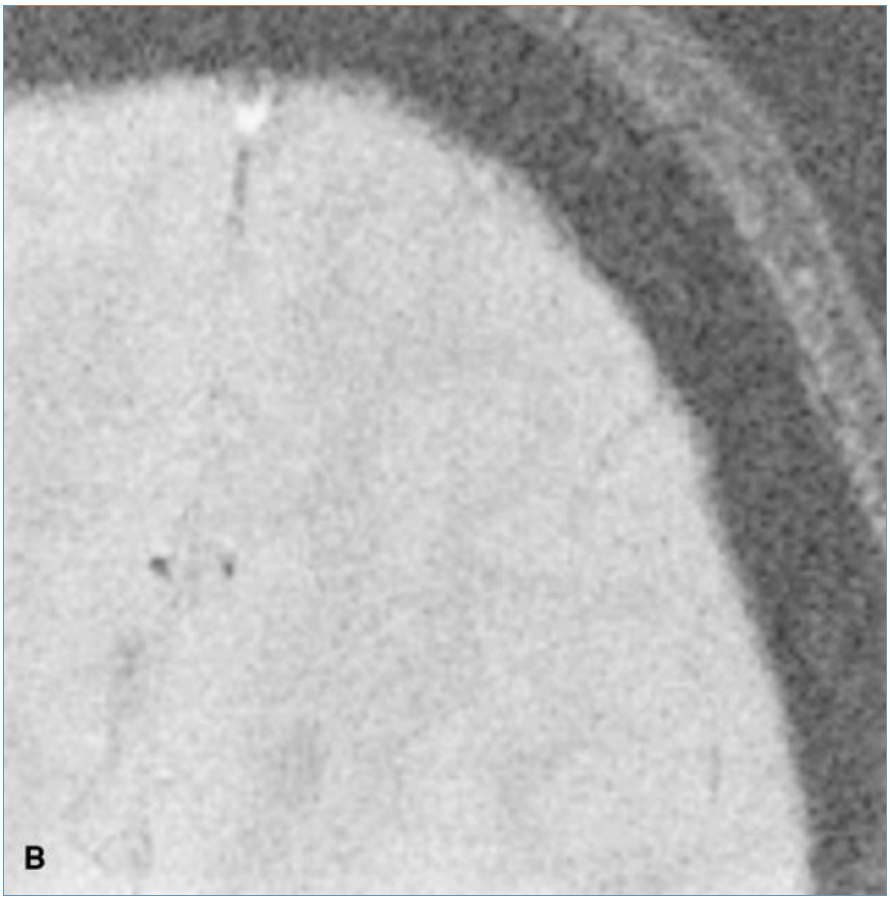

Figure 1. Continued

In Fig. 2A, the first 2,000 × 2,000 image of the human head is presented. A section of this gradient echo axial image is expanded 10-fold in Fig. 2B. The image displayed in Fig. 2 was obtained with a 2 mm slice thickness from a

image is expanded 10-fold in Fig. 2B. The image displayed in Fig. 2 was obtained with a 2 mm slice thickness from a 20 cm FOV using 1 NEX and full k-space sampling. This resulted in an in-plane resolution of 100 µm, a pixel volume of only 0.02 mm^3, and a signal to noise of approximately 20:1.

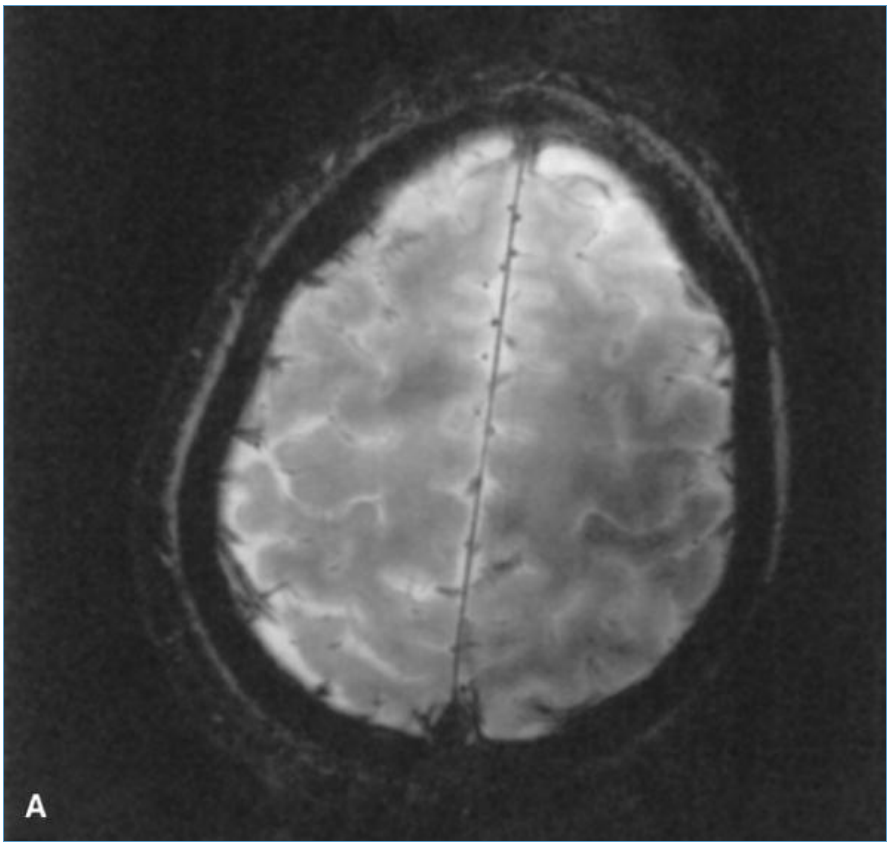

FIG. 2. A: Axial gradient recalled echo image acquired in 23 minutes at 8 Tesla using a TEM resonator (40,46) operating in quadrature (matrix size = 2,000 × 2,000, slice thickness = 2,000 µm, FOV = 20 cm, in-plane resolution = 100 µm, TR = 750 ms, TE = 17 ms, receiver bandwidth = 69.4 kHz, slices = 6, NEX = 1, flip angle = 45°). **B:** Expanded view of the image displayed in (A). Despite the use of a larger receiver bandwidth and matrix size, this 8 Tesla image has a signal to noise of 20:1.

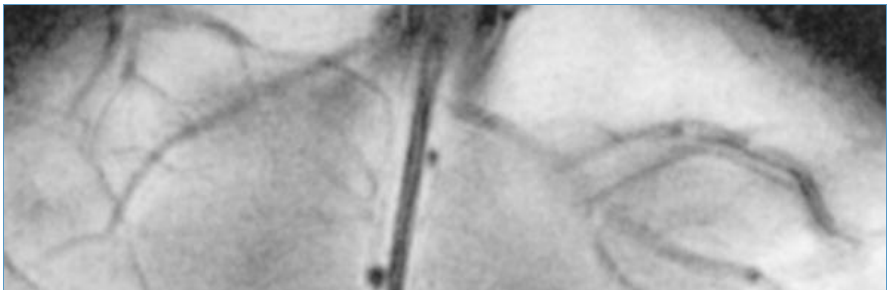

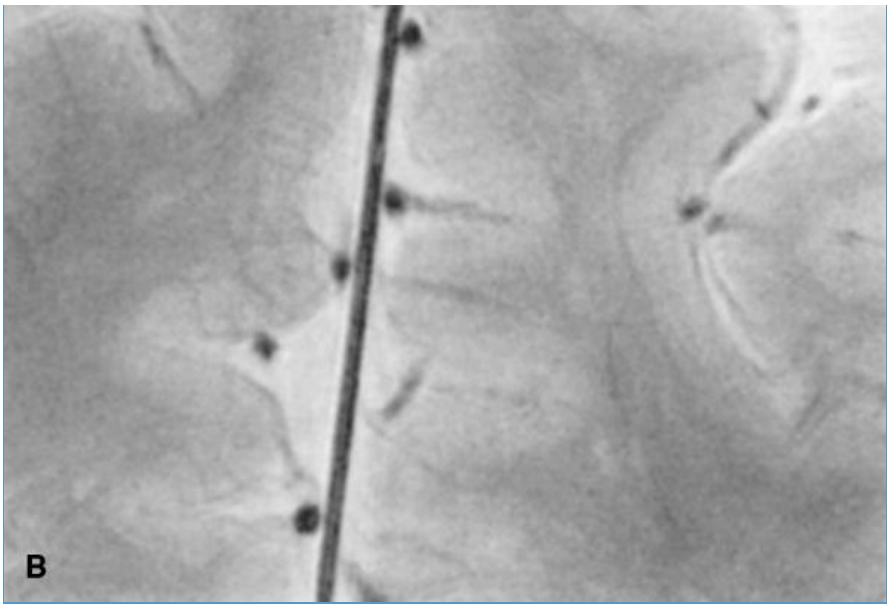

Figure 2. Continued

Three additional sections of ultra high resolution images obtained with a sagital orientation are displayed in Fig. 3. Once again these images were obtained with a 2,000 × 2,000 matrix size from a 20 cm FOV using a 2 mm slice thickness. Note the tremendous degree of vascular detail in each of these expanded views.

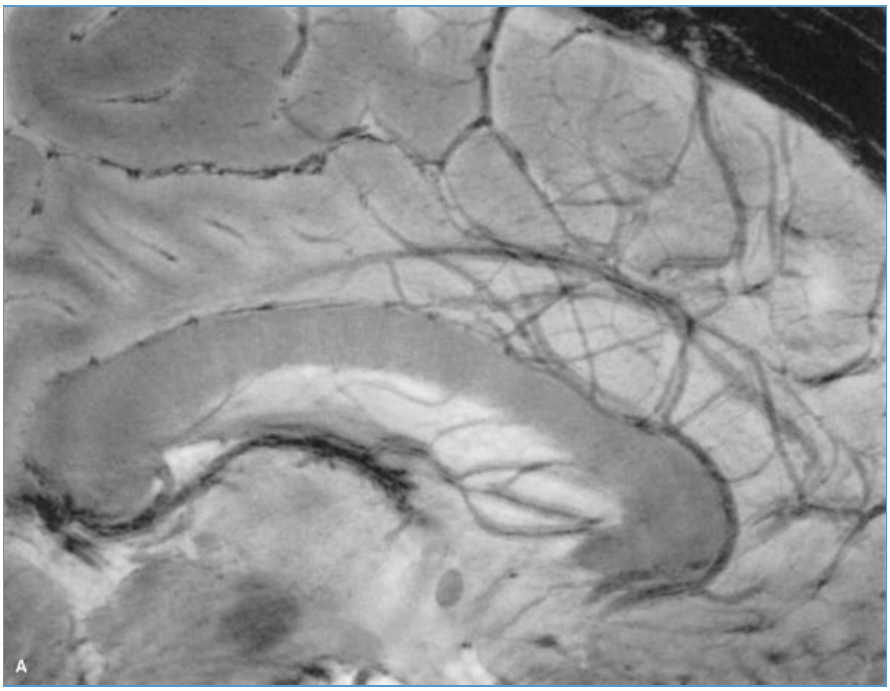

FIG. 3. A,B (*opposite page*), **and C:** Expanded views of sagittal gradient recalled echo images obtained at 8 Tesla using a TEM resonator (40,46) operating in quadrature (matrix size = 2,000 × 2,000, slice thickness = 2,000 µm, FOV = 20 cm, in-plane resolution = 100 µm, TR = 750 ms, TE = 17 ms, receiver bandwidth = 69.4 kHz, slices = 6, NEX = 1, flip angle = 45°). Note the excellent vascular details.

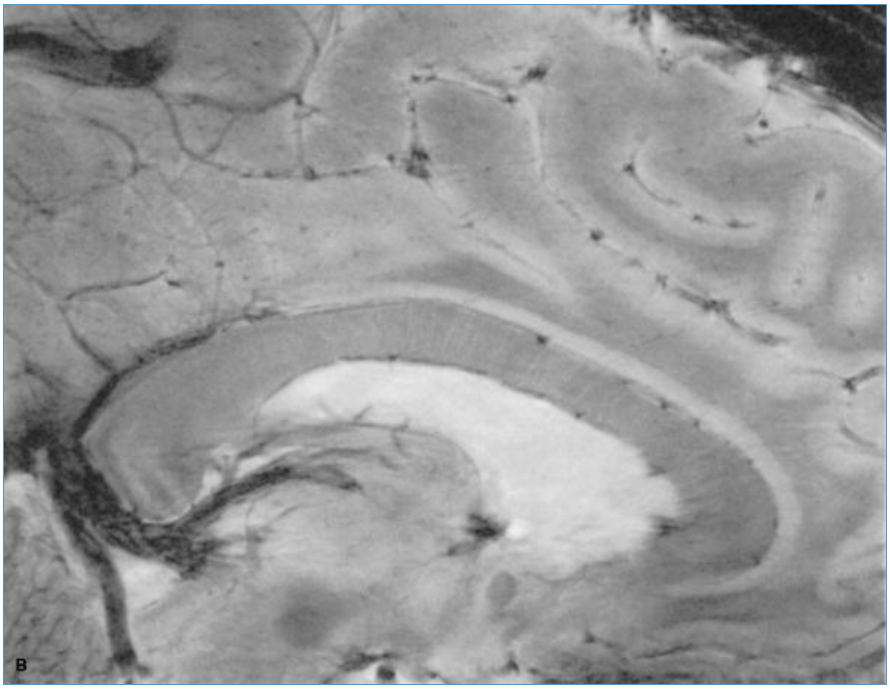

Figure 3. Continued

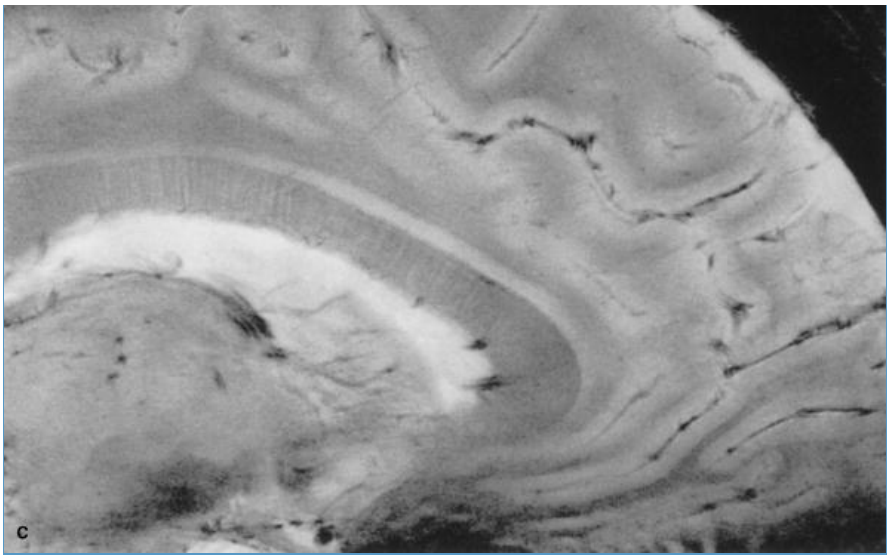

Figure 3. Continued

DISCUSSION

Given the excellent technological performance of modern MRI scanners, the ability to acquire ultra high resolution images with this modality is governed almost exclusively by available signal to noise. Thus, while excellent images can be acquired at 1.5 Tesla (38,39), this field strength lacks the inherent signal to noise to make ultra high resolution imaging (pixel volume <= 0.02 mm^3) feasible. As such, note that when conventional acquisition methods are utilized at 1.5 Tesla (see Fig. 1), it is difficult to obtain a resolution with a pixel volume much below 0.3 mm^3. Indeed, using a standard gradient echo sequence and head coil configuration with a state-of-the-art clinical scanner, images obtained with a 0.3 mm^3 pixel volume yielded little or no useful diagnostic information. In contrast, at 8 Tesla, ultra high resolution images (pixel volume <= 0.02 mm^3) can be obtained using standard imaging sequences and RF head coils without difficulty. This is the case despite the use of larger receiver bandwidths and less than fully relaxed spin excitation conditions.

The image displayed in Fig. 2 was presented for historical reasons in that it represents the first attempt to obtain ultra high resolution results at 8 Tesla (44,48). Nonetheless, while this image does not possess good contrast, it does reveal the potential of ultra high frequency magnetic resonance imaging (UHFMRI) for increasing spatial resolution. While the 1.5 Tesla image displayed in Fig. 1 was characterized with a signal-to-noise ratio of about 6:1, the 8 Tesla image revealed a signal-to-noise ratio of approximately 20:1—this despite the fact that the 1.5 Tesla image had only 1/16 the resolution of the 8 Tesla image and was acquired with a receiver bandwidth of 32 kHz. In contrast, the 8 Tesla image was acquired with a bandwidth of nearly 70 kHz. Indeed, the quality of the 8 Tesla image is somewhat surprising considering that it was compromised by larger receiver bandwidths and suboptimal excitation and relaxation parameters relative to the 1.5 Tesla image. Nonetheless, it remained superior in terms of signal to noise.

Additional ultra high resolution images were displayed in Fig. 3A–C. Note the vascular detail in these images, despite the use of a standard gradient echo sequence. Much of this vascular anatomy is venous in origin (42,43). Nonetheless, there are literally hundreds of minute vessels visible in these images. This speaks to the tremendous potential of UHFMRI in obtaining ultra high-resolution MRA results in the future. At the same time, while the pixel resolution on these images is outstanding, it cannot be directly related to true in-plane resolution due to inherent physiological motion. Thus, it may become important to gate image acquisition to cardiac or other physiological motion in order to help ensure that pixel resolution can be directly correlated to true resolution.

Nonetheless, the ability to obtain ultra high resolution images will remain ultimately dictated by the Boltzmann equation. This equation determines the distribution of the spin population in the up state relative to the down state as a result of temperature and field strength. Thus, given adequate spectrometer hardware, the only way to significantly enhance signal to noise is through a substantial increase in field strength. This has been confirmed with the recent assembly of an UHF 8 Tesla MRI system (44–46). Indeed, initial fast low angle shot (FLASH) images obtained on this system revealed a signal to noise in excess of 20 times that observed on a conventional GE Signa scanner (49).

The fundamental promise of UHFMRI (44–46) relies on increased image resolution and decreased scanning

times, both of which are critically related to intrinsic signal to noise (50). It reflects signal to noise in the absence of T1, T2*, motion, flow, and scanner hardware effects (50). Intrinsic signal to noise (50), in turn, must increase with field strength. The intrinsic signal to noise at 8 Tesla relative to 1.5 Tesla has yet to be formally reported. Nonetheless, it is clear from the images contained herein that the intrinsic signal to noise ratio (ISNR) at 8 Tesla will be phenomenal, possibly approaching a factor of 30 increase over a conventional 1.5 T scanner. Given such performance, it is difficult to fully visualize the potential impact of UHFMRI. Nonetheless, should the present trends in signal to noise and high resolution imaging continue (38,39,42,43), it appears that the radiological sciences are destined to become increasingly histological in nature.

Acknowledgment:

We thank Ying Yu, Ryan Gilbert, and Amy Daniels for their valuable assistance. This work was supported in part by NIH grant HL 45120.

REFERENCES

1. Damadian R, Goldsmith M, Minkoff L. NMR scanning. In:*NMR Basic Principles and Progress.* vol. 19. Diehl P, Fluck E, Kosfeld R, eds. Berlin: Springer-Verlag, 1981:1–16. [Context Link]

2. Lauterbur PC. Image formation by induced local interactions: example employing nuclear magnetic resonance. Nature 1973; 242:190–1. **UWA Library Holdings** | [Context Link]

3. Mansfield P, Chapman B. Active magnetic screening of gradient coils in NMR imaging. J Magn Reson 1986; 66:573–6. **UWA Library Holdings** | [Context Link]

4. Kumar A, Welti D, Ernst RR. NMR Fourier Zeugmatography. J Magn Reson 1975; 18:69–83. **UWA Library Holdings** | [Context Link]

5. Edelstein WA, Hutchison JMS. Spin warp NMR imaging and applications to human whole-body imaging. Phys Biol Med 1990; 25:751–6. [Context Link]

6. Young IR, Cox IJ, Bryant D, Bydder GM. The benefits of increasing spatial resolution as a means of reducing susceptibility artifacts due to field inhomogeneities. Magn Reson Imag 1988; 6:585–90. **UWA Library Holdings** | [Context Link]

7. Abduljalil AM, Robitaille P-ML. Macroscopic susceptibility in ultra high field MRI. J Comput Assist Tomogr 1999; 23:832–41. **Ovid Full Text** | **UWA Library Holdings** | [Context Link]

8. Constable RT, Henkelman RM. Contrast, resolution, and detectability in MR imaging. J Comput Assist Tomogr 1991; 15:297–303. **Ovid Full Text** | **UWA Library Holdings** | [Context Link]

9. Venkatesan R, Haacke EM. Role of high resolution in magnetic resonance (MR) imaging: applications to MR angiography, intracranial T1-weighted imaging, and image interpolation. Int J Imag Sys Technol 1997; 8:529–43. [Context Link]

10. Edelstein WA, Glover GH, Hardy CJ, Redington RW. The intrinsic signal-to-noise in NMR imaging. Magn Reson Med 1986; 3:604–18. **UWA Library Holdings** | [Context Link]

11. Parker DL, Gullberg GT. Signal to noise efficiency in magnetic resonance imaging. Med Phys 1990; 17:250–7. [Context Link]

12. Hoult DI, Richards RE. The signal to noise of the nuclear magnetic resonance experiment. J Magn Reson 1976; 24:71–85. [Context Link]

13. Ackerman JJH, Grove TH, Wong GG, Gadian DG, Radda GK. Mapping of metabolites in whole animals by 31P NMR using surface coils. Nature 1980; 283:167–70. **UWA Library Holdings** | [Context Link]

14. Roemer PB, Edelstein WA, Hayes CE, Souza SP, Meuller OM. The NMR phased array. Magn Reson Med 1990; 16:192–225. **UWA Library Holdings** | [Context Link]

15. McVeigh ER, Henkelman RM, Bronskill MJ. Noise and filtration in magnetic resonance imaging. Med Phys 1985; 12:586–91. **UWA Library Holdings** | [Context Link]

16. Ying K, Clymer BD, Schmalbrock P. Adaptive filtering for high resolution magnetic resonance images. J Magn Reson Imag 1996; 6:367–77. **UWA Library Holdings** | [Context Link]

17. Idy-Peretti I, Bittoun J, Alliot FA, Richard SB, Querleux BG, Cluzan RV. Lymphedematous skin and subcutis: in vivo high resolution magnetic resonance imaging evaluation. J Invest Dermatol 1998; 110:782—7. [Context Link]

18. Potter HG, Asnis-Ernberg L, Weiland AJ, Hotchkiss RN, Peterson MGE, McCormack RR. The utility of high-resolution magnetic resonance imaging in the evaluation of the triangular fibrocartilage complex of the wrist. J Bone Joint Surg 1997; 79A:1675–84. [Context Link]

19. Drape JL, Peretti I, Goettmann S, Guerin-Surville H, Bittoun J. Standard and high resolution magnetic resonance imaging of glomus tumors of toes and fingertips. J Am Acad Dermatol 1996; 35:550–5. **UWA Library Holdings** | [Context Link]

20. Waldschmidt JG, Rilling RJ, Kajdacsy-Balla AA, Boynton MD, Erickson SJ. In vitro and in vivo MR imaging of hyaline cartilage: zonal anatomy, imaging pitfalls, and pathologic conditions. Radiograph 1997; 17:1387–1402. [Context Link]

21. Majumdar S, Genant HK, Grampp SS, Newitt DC, Truong VH, Lin JC, Mathur A. Correlation of trabecular bone structure with age, bone mineral density, and osteoporotic status: in vivo studies in the distal radius using high resolution magnetic resonance imaging. J Bone Mineral Res 1997; 12:111–18. **UWA Library Holdings** | [Context Link]

22. Ouyang X, Selby K, Lang P, et al. High resolution magnetic resonance imaging of the calcaneous: age-related changes in trabecular structure and comparison with dual X-ray absorptiometry measurements. Calcif Tissue Int 1997; 60:139–47. **UWA Library Holdings** | [Context Link]

23. Schmalbrock PM, Pruski J, Sun L, Rao A, Monroe J. Phased array RF coils for high-resolution MRI of the inner ear and brain stem. J Comput Assist Tomogr 1995; 19:8–14. **Ovid Full Text** | **UWA Library Holdings** | [Context Link]

24. Brogan M, Chakeres DW, Schmalbrock P. High-resolution 3DFT MR imaging of the endolymphatic duct and soft tissue of the otic capsule. AJNR 1991; 12:1–11. **UWA Library Holdings** | [Context Link]

25. Arnold B, Jager L, Grevers G. Visualization of inner ear structures by three-dimensional high resolution magnetic resonance imaging. Am J Otol 1996; 17:480–5. **Ovid Full Text** | **UWA Library Holdings** | [Context Link]

26. Dahm MC, Mack MG, Tykocinski M, Vogl TJ. Submillimeter imaging and reconstruction of the inner ear. Am J Otol 1997; 18:S54–S56. **Ovid Full Text** | **UWA Library Holdings** | [Context Link]

27. Casselman JW, Kuhweide R, Deimling M, Ampe W, Dehaeme I, Meeus L. Constructive interference in steady state-3DFT MR imaging of the inner ear and cerebellopontine angle. AJNR 1993; 14:47–57. [Context Link]

28. Ettl A, Kramer J, Daxer A, Koornneef L. High-resolution magnetic resonance imaging of the normal extraocular musculature. Eye 1997; 11:93–7. **UWA Library Holdings** | [Context Link]

29. Mashima Y, Oshitari K, Imamura Y, Momoshima S, Shiga H, Oguchi Y. Orbital high resolution magnetic resonance imaging with fast spin echo in the acute stage of Leber's hereditary optic neuropathy. J Neurol Neurosurg Psychiatry 1998; 64:124–7. **UWA Library Holdings** | [Context Link]

30. Herrick RC, Hayman LA, Taber KH, Diaz-Marchan PJ, Kuo MD. Artifacts and pitfalls in MR imaging of the orbit: a clinical review. Radiograph 1997; 17:707–24. [Context Link]

31. Gass A, Barker GJ, MacManus D, et al. High resolution magnetic resonance imaging of the anterior visual pathway in patients with optic neuropathies using fast spin echo and phased array local coils. J Neurol Neurosurg Psychiatry 1995; 58:562–9. **UWA Library Holdings** | [Context Link]

32. Miloro M. Halkias LE, Slone HW, Chakeres DW. Assessment of the lingual nerve in the third molar region using magnetic resonance imaging. J Oral Maxillofac Surg 1997; 55:134–7. **UWA Library Holdings** | [Context Link]

33. Dailiana T, Chakeres D, Schmalbrock P, Williams P, Aletras A. High resolution MR of the intraparotid facial nerve and parotid duct. AJNR 1997; 18:165–72. [Context Link]

34. McGhee RB, Chakeres DW, Schmalbrock P, Brogan MA, Negulesco JA. The extracranial facial nerve: high resolution three-dimensional Fourier transform MR imaging. AJNR 1993; 14:465–72. **UWA Library Holdings** | [Context Link]

35. Laub GA, Kaiser WA. MR angiography with gradient motion refocusing. J Comput Assist Tomogr 1988; 12:377–82. **Ovid Full Text** | **UWA Library Holdings** | [Context Link]

36. Parker DL, Parker DJ, Blatter DD, Du YP, Goodrich KC. The effect of image resolution on vessel signal in high resolution magnetic resonance angiography. J Magn Reson Imag 1996; 6:632–41. **UWA Library Holdings** | [Context Link]

37. Barth M, Reichenbach JR, Vaenkatesan R, Moser E, Haacke EM. High-resolution, multiple gradient-echo functional MRI at 1.5 T. Magn Reson Imag 1999; 17:321–9. [Context Link]

38. Wald LL, Carvajal L, Moyer SE, Nelson SJ, Grant PE, Barkovich AJ, Vigneron DB. Phased array detectors and an automated intensity-correction algorithm for high-resolution MR imaging of the human brain. Magn Reson Med 1995; 34:433–9. **UWA Library Holdings** | [Context Link]

39. Feinberg DA, Kiefer B, Litt AW. High resolution GRASE MRI of the brain and spine: 512 and 1024 matrix imaging. J Comput Assist Tomogr 1995; 19:1–7. **Ovid Full Text** | **UWA Library Holdings** | [Context Link]

40. Vaughan JT, Hetherington HP, Otu JO, Pan JW, Pohost GM. High frequency volume coils for clinical NMR imaging and spectroscopy. Magn Reson Med 1994; 32:206–18. **UWA Library Holdings** | [Context Link]

41. Pan JW, Vaughan JT, Kuzniecky RI, Pohost GM, Hetherington HP. High resolution neuroimaging at 4.1 T. Magn Reson Imag 1995; 13:915–21. **UWA Library Holdings** | [Context Link]

42. Christoforidis GA, Bourekas EC, Baujan M, Abduljalil AM, Kangarlu A, Spigos DG, Chakeres DW, Robitaille P-ML. High resolution MRI of the deep brain vascular anatomy at 8 Tesla: susceptibility-based enhancement of the venous structures. J Comput Assist Tomogr 1999; 23;857–66. [Context Link]

43. Burgess RE, Yu Y, Christoforidis GA, Bourekas EC, Chakeres DW, Spigos D, Kangarlu A, Abduljalil AM, Robitaille P-ML. Human leptomeningeal and cortical vascular anatomy of the cerebral cortex at 8 Tesla. J Comput Assist

Tomogr 1999; 23:850–56. **Ovid Full Text** | **UWA Library Holdings** | [Context Link]

44. Robitaille P-ML, Abduljalil AM, Kangarlu A, et al. Human magnetic resonance imaging at 8 T. NMR Biomed 1998; 11:1–3. **UWA Library Holdings** | [Context Link]

45. Robitaille P-ML, Warner R, Jagadeesh J, et al. Design and assembly of an 8 Tesla whole-body MR scanner. J Comput Assist Tomogr 1999; 23:808–20. **Ovid Full Text** | **UWA Library Holdings** | [Context Link]

46. Robitaille P-ML. Black-body and transverse electromagnetic resonators operating at 340 MHz: volume RF coils for ultra high field MRI. J Comput Assist Tomogr 1999; 23:879–90. **Ovid Full Text** | **UWA Library Holdings** | [Context Link]

47. Abduljalil AM, Aletras AH, Robitaille P-ML. Torque free asymmetric gradient coils for echo planar imaging. Magn Reson Med 1994; 31:450–3. **UWA Library Holdings** | [Context Link]

48. Robitaille P-ML. On RF power and dielectric resonances in UHFMRI. NMR Biomed 1999; 12:318–19. **UWA Library Holdings** | [Context Link]

49. Burgess RE, Yu Y, Abduljalil AM, Kangarlu A, Robitaille P-ML. High signal to noise FLASH imaging at 8 Tesla. Magn Reson Imag 1999; 17:1099–1103. **UWA Library Holdings** | [Context Link]

50. Edelstein WA, Glover GH, Hardy CJ, Redington RW. The intrinsic signal to noise ratio in NMR imaging. Magn Reson Med 1986; 3:604–18. **UWA Library Holdings** | [Context Link]

Key Words: Magnetic resonance imaging; High resolution; Brain; Microanatomy; Atlas and atlases

---

IMAGE GALLERY

Select All **Export Selected to PowerPoint**

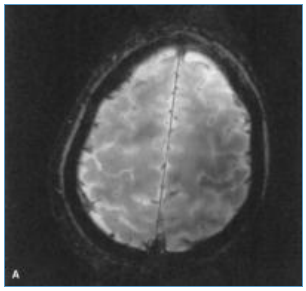

Fig. 2

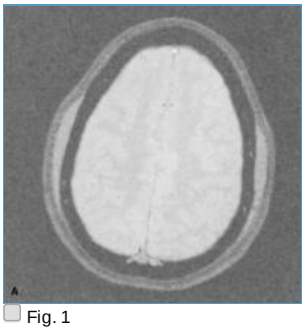

Fig. 1

Figure 1

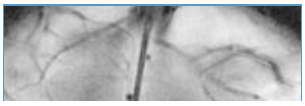

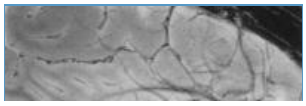

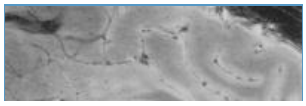

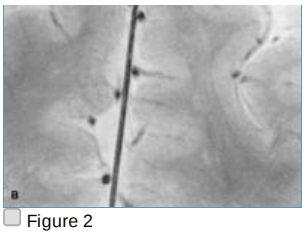
Figure 2

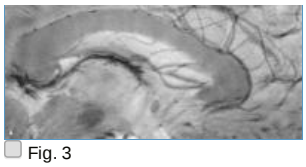
Fig. 3

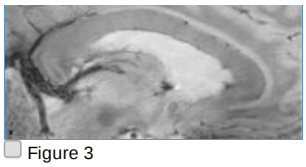
Figure 3

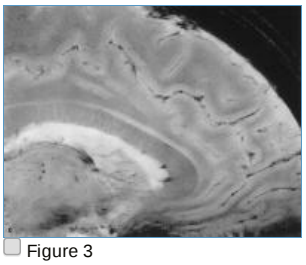
Figure 3

Back to Top